

# Performance Impact of Base Station Antenna Heights in Dense Cellular Networks

Ming Ding, *Member, IEEE*, David López-Pérez, *Member, IEEE*

## Abstract

In this paper, we present a new and significant theoretical discovery. If the absolute height difference between base station (BS) antenna and user equipment (UE) antenna is larger than zero, then the network performance in terms of both the coverage probability and the area spectral efficiency (ASE) will *continuously decrease* toward zero as the BS density increases for ultra-dense (UD) small cell networks (SCNs). Such findings are completely different from the conclusions in existing works, both quantitatively and qualitatively. In particular, this performance behavior has a tremendous impact on the deployment of UD SCNs in the 5th-generation (5G) era. Network operators may invest large amounts of money in deploying more network infrastructure to only obtain an even less network capacity. Our study results reveal that one way to address this issue is to lower the SCN BS antenna height to the UE antenna height. However, this requires a revolutionized approach of BS architecture and deployment, which is explored in this paper too.

## I. INTRODUCTION

From 1950 to 2000, the wireless network capacity has increased around 1 million fold, in which an astounding  $2700\times$  gain was achieved through network densification using smaller cells [1]. In the first decade of 2000, network densification continued to fuel the 3rd Generation Partnership Project (3GPP) 4th-generation (4G) Long Term Evolution (LTE) networks, and is expected to remain as one of the main forces to drive the 5th-generation (5G) networks onward [2]. Indeed, the orthogonal deployment of ultra-dense (UD) small cell networks (SCNs) within the existing macrocell network, i.e., small cells and macrocells operating on different frequency spectrum (3GPP Small Cell Scenario #2a [3]), is envisaged as the

Ming Ding is with Data61, CSIRO, Australia (e-mail: Ming.Ding@data61.csiro.au).

David López-Pérez is with Nokia Bell Labs, Ireland (email: david.lopez-perez@nokia-bell-labs.com).

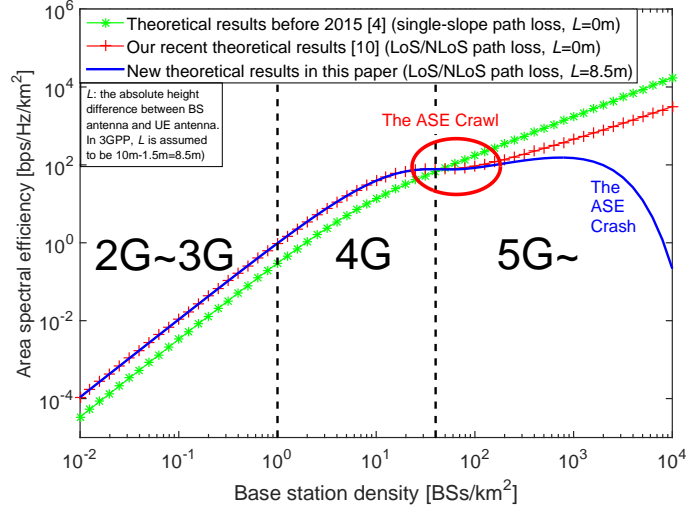


Fig. 1. Theoretical comparison of the ASE performance in  $\text{bps/Hz/km}^2$ . Note that all the results are obtained using practical 3GPP channel models [5], [6], which will be introduced later. Due to the practicality of the used channel models, the results shown here accurately characterize the realistic telecommunication systems both qualitatively and quantitatively. For example, considering a typical bandwidth of 10 MHz~100 MHz for the state-of-the-art LTE network, the achievable area throughput is in the order of several Gbps/km<sup>2</sup>, because the ASE for 4G is shown to be around 100 bps/Hz/km<sup>2</sup>.

workhorse for capacity enhancement in 5G due to its large spectrum reuse and its easy management; the latter one arising from its low interaction with the macrocell tier, e.g., no inter-tier interference [2]. In this paper, the focus is on the analysis of these UD SCNs with an orthogonal deployment with the macrocells.

Before 2015, the common understanding on SCNs was that the density of base stations (BSs) would not affect the per-BS coverage probability performance in interference-limited fully-loaded wireless networks, and thus the area spectral efficiency (ASE) performance in  $\text{bps/Hz/km}^2$  would scale linearly with the network densification [4]. The implication of such conclusion is huge: *The BS density does NOT matter*, since the increase in the interference power caused by a denser network would be exactly compensated by the increase in the signal power due to the reduced distance between transmitters and receivers. Fig. 1 shows the theoretical ASE performance predicted in [4] across the typical BS density regions for various generations of telecommunication systems. However, it is important to note that this conclusion in [4] was obtained with considerable simplifications on the propagation environment, which should be placed under scrutiny when evaluating dense and UD SCNs, since they are fundamentally different from sparse ones in various aspects [2].

In the past year, a few noteworthy studies have been carried out to revisit the network performance analysis for dense and UD SCNs under more practical propagation assumptions. In [7], the authors considered a multi-slope piece-wise path loss function, while in [8],

the authors investigated line-of-sight (LoS) and non-line-of-sight (NLoS) transmission as a probabilistic event for a millimeter wave communication scenario. The most important finding in these two works was that the per-BS coverage probability performance starts to decrease when the BS density is sufficiently large. Fortunately, such decrease of coverage probability did not change the monotonic increase of the ASE as the BS density increases.

In our very recent work [9], [10], we took a step further and generalized the works in [7] and [8] by considering both piece-wise path loss functions and probabilistic NLoS and LoS transmissions. Our new finding was not only quantitatively but also qualitatively different from previous results in [4], [7], [8]: The ASE will suffer from a slow growth or even a small *decrease* on the journey from 4G to 5G when the BS density is larger than a threshold. Fig. 1 shows these new theoretical results on the ASE performance, where such threshold is around 20 BSs/km<sup>2</sup> and the slow/negative ASE growth is highlighted by a circled area. This circled area is referred to as *the ASE Crawl* hereafter. The intuition of *the ASE Crawl* is that the interference power increases faster than the signal power due to the transition of a large number of interference paths from NLoS to LoS with the network densification. The implication is profound: *The BS density DOES matter*, since it affects the signal to interference relationship in terms of the power ratio. As a result, network operators should be careful when deploying dense SCNs in order to avoid investing huge amounts of money and end up obtaining an even worse network performance due to *the ASE Crawl*. Fortunately, our results in [9], [10] also pointed out that the ASE will again grow almost linearly as the network further evolves to an UD SCN, e.g.,  $> 10^3$  BSs/km<sup>2</sup> in Fig. 1.

Unfortunately, the NLoS to LoS transition of interfering paths is not the only obstacle to efficient UD SCNs in 5G, and there are more challenges to overcome to get there. In this paper, we present the serious problem posed by the absolute antenna height difference between SCN BSs and user equipments (UEs), and evaluate its impact on UD SCNs by means of a three-dimensional (3D) stochastic geometry analysis (SGA). We made a new and significant theoretical discovery: If the absolute antenna height difference between BSs and UEs, denoted by  $L$ , is larger than zero, then the ASE performance will *continuously decrease* toward zero as the SCN goes ultra-dense. Fig. 1 illustrates the significance of

such theoretical finding with  $L = 8.5\text{ m}$ <sup>1</sup>: After *the ASE Crawl*, the ASE performance only increases marginally ( $\sim 1.4\times$ ) from  $109.1\text{ bps/Hz/km}^2$  to  $149.6\text{ bps/Hz/km}^2$  as the BS density goes from  $200\text{ BSs/km}^2$  to  $10^3\text{ BSs/km}^2$ , which is then followed by a continuous and quick fall to zero starting from around  $10^3\text{ BSs/km}^2$ . The implication of this result is even more profound than that of *the ASE Crawl*, since following a traditional deployment with UD SCN BSs deployed at lamp posts or similar heights will dramatically reduce the network performance in 5G<sup>2</sup>. Such decline of ASE in UD SCNs will be referred to as *the ASE Crash* hereafter, and its fundamental reasons will be explained in detail later in this paper.

In order to address the problem of *the ASE Crash*, we propose to lower the 5G UD SCN BS antenna height, not just by a few meters, but straight to the UE antenna height, so that the ASE behavior of UD SCNs can roll back to our previous results in [10]. However, this brings revolutionized BS deployments and new hardware issues, which will be discussed later.

Note that preliminary results of our work will be presented in a conference paper [12]. Compared with [12], the additional contributions of this journal version of our work are:

- We present the derivation of the analytical results on the coverage probability and the ASE performance considering the absolute antenna height difference between BSs and UEs. Note that in [12], we omitted the mathematical derivation due to the page limitation.
- Using the above results, assuming a general path loss model and considering the absolute height difference, numerically tractable integral-form expressions for the coverage probability and the ASE are further obtained for a 3GPP path loss model with a *linear* LoS probability function. Our analysis can be readily extended to deal with more complicated path loss models by approximating the corresponding LoS probability function as a piece-wise *linear* function.
- We provide the proof for our theoretical discovery. Note that in [12], we didn't provide the proof of *the ASE Crash* due to the page limitation.
- We show new numerical and simulation results to investigate the impacts of several factors on the existence/severity of *the ASE Crash*, e.g., an alternative 3GPP path loss model, various values of the absolute antenna height difference, Rician fading, practical

<sup>1</sup>The BS antenna height and the UE antenna height are assumed to be 10 m and 1.5 m, respectively [11].

<sup>2</sup>It is very important to note that, compared with the existing works with  $L = 0\text{ m}$  [9], [10], our new discovery has been achieved by changing nothing but adopting the more practical 3GPP assumption that  $L = 8.5\text{ m}$  [11].

antenna pattern and downtilt, etc.

The rest of this paper is structured as follows. Section II provides a brief review on the related work. Section III describes the system model for the 3D SGA. Section IV presents our theoretical results on the coverage probability and the ASE performance, with their application in a 3GPP special case addressed in Appendix C. The numerical results are discussed in Section V, with remarks shedding new light on the revolutionized UD SCN BS deployment with UE-height antennas. Finally, the conclusions are drawn in Section VI.

## II. RELATED WORK

In stochastic geometry, BS positions are typically modeled as a Homogeneous Poisson Point Process (HPPP) on the plane, and closed-form expressions of coverage probability can be found for some scenarios in single-tier cellular networks [4] and multi-tier cellular networks [13]. The major conclusion in [4], [13] is that neither the number of cells nor the number of cell tiers changes the coverage probability in interference-limited fully-loaded wireless networks. Recently, a few noteworthy studies have been carried out to revisit the network performance analysis for dense and UD SCNs. As have discussed in Section I, the authors of [7] and [8] found that the per-BS coverage probability performance will start to decrease when the BS density is sufficiently large. In our very recent work [9], [10], we presented a new finding that the ASE will suffer from a slow growth or even a small *decrease* on the journey from 4G to 5G when the BS density is larger than a threshold, i.e., *the ASE Crawl*. However, none of the above works considered the antenna heights of BSs and UEs in the theoretical analysis, which will be the focus of this work. It is very important to note that the authors of [14], [15] recently proposed a new approach of network performance analysis based on HPPP intensity matching. Such new approach may also be used to investigate the BS antenna height issue, and it is interesting to conduct a comparison study on the intensity matching approach and our analysis in terms of the accuracy loss due to approximation and the computational complexity, etc. In this work, we will focus on revealing *the ASE Crash* phenomenon using the traditional framework developed in [7]–[10].

Another research area relating to the antenna height issue is that of unmanned aerial vehicles (UAVs), which has attracted significant attention as key enablers for rapid network deployment. For example, in [16], a new form of mobile Ad hoc networks with special

characteristics like mobility, channel model, and energy consumption was defined as the Flying Ad hoc Networks (FANET). In [17], the authors considered one drone BS and investigated the optimum trajectory and heading of the drone BS for a multi-UE ground to air uplink scenario. In a recent work [18], the authors considered a two-drone scenario and studied the problem of providing a maximum coverage for a certain geographical area. Generally speaking, the works on drone BSs put a lot of emphasis on the 3D mobility of UAVs and try to numerically find the optimal position/height for the drone deployment in a small area involving just a few flying BSs. In contrast, our work considers a large-scale, randomly-deployed and stationary cellular network, paying special attention to the theoretical capacity performance for the whole network.

### III. SYSTEM MODEL

We consider a downlink (DL) cellular network with BSs deployed on a plane according to a homogeneous Poisson point process (HPPP)  $\Phi$  with a density of  $\lambda$  BSs/km<sup>2</sup>. Note that the value of  $\lambda$  is in the order of 10~100 for the current 4G networks [5]. UEs are Poisson distributed in the considered network with a density of  $\rho$  UEs/km<sup>2</sup>. Note that  $\rho$  is assumed to be sufficiently larger than  $\lambda$  so that each BS has at least one associated UE in its coverage [7]–[10]. The two-dimensional (2D) distance between a BS and an a UE is denoted by  $r$ . Moreover, the absolute antenna height difference between a BS and a UE is denoted by  $L$ . Note that the value of  $L$  is in the order of several meters. As discussed in Section I, for the current 4G networks,  $L$  is around 8.5 m because the BS antenna height and the UE antenna height are assumed to be 10 m and 1.5 m, respectively [11]. Hence, the 3D distance between a BS and a UE can be expressed as

$$w = \sqrt{r^2 + L^2}. \quad (1)$$

Note that an alternative method is to present the 3D distance in polar coordinates as in [19].

Following [9], [10], we adopt a very general path loss model, in which the path loss  $\zeta(w)$  associated with distance  $w$  is segmented into  $N$  pieces written as

$$\zeta(w) = \begin{cases} \zeta_1(w), & \text{when } 0 \leq w \leq d_1 \\ \zeta_2(w), & \text{when } d_1 < w \leq d_2 \\ \vdots & \vdots \\ \zeta_N(w), & \text{when } w > d_{N-1} \end{cases}, \quad (2)$$

where each piece  $\zeta_n(w)$ ,  $n \in \{1, 2, \dots, N\}$  is modeled as

$$\zeta_n(w) = \begin{cases} \zeta_n^L(w) = A_n^L w^{-\alpha_n^L}, & \text{LoS: } \Pr_n^L(w) \\ \zeta_n^{\text{NL}}(w) = A_n^{\text{NL}} w^{-\alpha_n^{\text{NL}}}, & \text{NLoS: } 1 - \Pr_n^L(w) \end{cases}, \quad (3)$$

where  $\zeta_n^L(w)$  and  $\zeta_n^{\text{NL}}(w)$ ,  $n \in \{1, 2, \dots, N\}$  are the  $n$ -th piece path loss functions for the LoS transmission and the NLoS transmission, respectively,  $A_n^L$  and  $A_n^{\text{NL}}$  are the path losses at a reference distance  $w = 1$  for the LoS and the NLoS cases, respectively, and  $\alpha_n^L$  and  $\alpha_n^{\text{NL}}$  are the path loss exponents for the LoS and the NLoS cases, respectively. In practice,  $A_n^L$ ,  $A_n^{\text{NL}}$ ,  $\alpha_n^L$  and  $\alpha_n^{\text{NL}}$  are constants obtainable from field tests [5], [6]. Moreover,  $\Pr_n^L(w)$  is the  $n$ -th piece LoS probability function that a transmitter and a receiver separated by a distance  $w$  has a LoS path, which is assumed to be a monotonically decreasing function with regard to  $w$  in this paper.

For convenience,  $\{\zeta_n^L(w)\}$  and  $\{\zeta_n^{\text{NL}}(w)\}$  are further stacked into piece-wise functions written as

$$\zeta^{\text{Path}}(w) = \begin{cases} \zeta_1^{\text{Path}}(w), & \text{when } 0 \leq w \leq d_1 \\ \zeta_2^{\text{Path}}(w), & \text{when } d_1 < w \leq d_2 \\ \vdots & \vdots \\ \zeta_N^{\text{Path}}(w), & \text{when } w > d_{N-1} \end{cases}, \quad (4)$$

where the string variable *Path* takes the value of “L” and “NL” for the LoS and the NLoS cases, respectively. Besides,  $\{\Pr_n^L(w)\}$  is also stacked into a piece-wise function as

$$\Pr^L(w) = \begin{cases} \Pr_1^L(w), & \text{when } 0 \leq w \leq d_1 \\ \Pr_2^L(w), & \text{when } d_1 < w \leq d_2 \\ \vdots & \vdots \\ \Pr_N^L(w), & \text{when } w > d_{N-1} \end{cases}. \quad (5)$$

In this paper, we assume a practical user association strategy (UAS), in which each UE is connected to the BS with the smallest path loss (i.e., with the largest  $\zeta(w)$ ) [8], [10]. Moreover, we assume that each BS/UE is equipped with an isotropic antenna, and that the multi-path fading between a BS and a UE is modeled as independently identical distributed (i.i.d.) Rayleigh fading [7]–[10]. In order to consider more realistic environments other than the general path loss functions, we further perform the following studies via simulations:

- A more practical Rician fading will be considered in Section V to show its impact on our conclusions. Note that the analytical results based on the assumption of Rician fading



can be derived following a similar logic as that in [20], which will be our future work.

- A more practical antenna pattern and downtilt will also be considered in Section V. Note that in practice each BS antenna has a 3D beam pattern and such beam will be electrically tilted downward to improve the signal power as well as reduce the inter-cell interference [21]–[23]. Intuitively speaking, the downtilt angle should increase with the network densification since each BS's effective coverage area shrinks. For example, the downtilt angle is around 10 degrees for macrocell BSs in [11] and it is significantly larger for SCN BSs [2].

#### IV. MAIN RESULTS

Using a 3D SGA based on the HPPP theory, we study the performance of the SCN by considering the performance of a typical UE located at the origin  $o$ .

##### A. The Coverage Probability

We first investigate the coverage probability  $p^{\text{cov}}(\lambda, \gamma)$  that the typical UE's signal-to-interference-plus-noise ratio (SINR) is above a per-designated threshold  $\gamma$ :

$$p^{\text{cov}}(\lambda, \gamma) = \Pr[\text{SINR} > \gamma], \quad (6)$$

where the SINR is calculated as

$$\text{SINR} = \frac{P\zeta(w)h}{I_{\text{agg}} + P_{\text{N}}}, \quad (7)$$

where  $h$  is the channel gain, modeled as an exponential random variable (RV) with the mean of one (due to our consideration of Rayleigh fading in this paper),  $P$  is the transmission power of each BS,  $P_{\text{N}}$  is the additive white Gaussian noise (AWGN) power at each UE, and  $I_{\text{agg}}$  is the cumulative interference given by

$$I_{\text{agg}} = \sum_{i: b_i \in \Phi \setminus b_o} P\beta_i g_i, \quad (8)$$

where  $b_o$  is the BS serving the typical UE at distance  $w$  from it,  $b_i$  is the  $i$ -th interfering BS, and  $\beta_i$  and  $g_i$  are the path loss and the multi-path fading channel gain of  $b_i$ , respectively.

Based on the proposed path loss model in (2) and the proposed UAS, we present our main result on the coverage probability  $p^{\text{cov}}(\lambda, \gamma)$  in Theorem 1.



**Theorem 1.** Considering the proposed path loss model in (2) and the proposed UAS, the probability of coverage  $p^{\text{cov}}(\lambda, \gamma)$  can be derived as

$$p^{\text{cov}}(\lambda, \gamma) = \sum_{n=1}^N (T_n^{\text{L}} + T_n^{\text{NL}}), \quad (9)$$

where  $T_n^{\text{L}} = \int_{\sqrt{d_{n-1}^2 - L^2}}^{\sqrt{d_n^2 - L^2}} \Pr\left[\frac{P\zeta_n^{\text{L}}(\sqrt{r^2 + L^2})h}{I_{\text{agg}} + P_{\text{N}}} > \gamma\right] f_{R,n}^{\text{L}}(r) dr$ ,  $T_n^{\text{NL}} = \int_{\sqrt{d_{n-1}^2 - L^2}}^{\sqrt{d_n^2 - L^2}} \Pr\left[\frac{P\zeta_n^{\text{NL}}(\sqrt{r^2 + L^2})h}{I_{\text{agg}} + P_{\text{N}}} > \gamma\right] f_{R,n}^{\text{NL}}(r) dr$ , and  $d_0$  and  $d_N$  are defined as  $L$  and  $+\infty$ , respectively. Moreover,  $f_{R,n}^{\text{L}}(r)$  and  $f_{R,n}^{\text{NL}}(r)$  ( $\sqrt{d_{n-1}^2 - L^2} < r \leq \sqrt{d_n^2 - L^2}$ ), are represented by

$$\begin{aligned} f_{R,n}^{\text{L}}(r) &= \exp\left(-\int_0^{r_1} \left(1 - \Pr^{\text{L}}(\sqrt{u^2 + L^2})\right) 2\pi u \lambda du\right) \\ &\quad \times \exp\left(-\int_0^r \Pr^{\text{L}}(\sqrt{u^2 + L^2}) 2\pi u \lambda du\right) \Pr_n^{\text{L}}(\sqrt{r^2 + L^2}) 2\pi r \lambda, \end{aligned} \quad (10)$$

and

$$\begin{aligned} f_{R,n}^{\text{NL}}(r) &= \exp\left(-\int_0^{r_2} \Pr^{\text{L}}(\sqrt{u^2 + L^2}) 2\pi u \lambda du\right) \\ &\quad \times \exp\left(-\int_0^r \left(1 - \Pr^{\text{L}}(\sqrt{u^2 + L^2})\right) 2\pi u \lambda du\right) \left(1 - \Pr_n^{\text{L}}(\sqrt{r^2 + L^2})\right) 2\pi r \lambda, \end{aligned} \quad (11)$$

where  $r_1$  and  $r_2$  are given implicitly by the following equations as

$$r_1 = \arg\left\{\zeta_n^{\text{NL}}(\sqrt{r_1^2 + L^2}) = \zeta_n^{\text{L}}(\sqrt{r^2 + L^2})\right\}, \quad (12)$$

and

$$r_2 = \arg\left\{\zeta_n^{\text{L}}(\sqrt{r_2^2 + L^2}) = \zeta_n^{\text{NL}}(\sqrt{r^2 + L^2})\right\}. \quad (13)$$

In addition,  $\Pr\left[\frac{P\zeta_n^{\text{L}}(\sqrt{r^2 + L^2})h}{I_{\text{agg}} + P_{\text{N}}} > \gamma\right]$  and  $\Pr\left[\frac{P\zeta_n^{\text{NL}}(\sqrt{r^2 + L^2})h}{I_{\text{agg}} + P_{\text{N}}} > \gamma\right]$  are respectively computed by

$$\Pr\left[\frac{P\zeta_n^{\text{L}}(\sqrt{r^2 + L^2})h}{I_{\text{agg}} + P_{\text{N}}} > \gamma\right] = \exp\left(-\frac{\gamma P_{\text{N}}}{P\zeta_n^{\text{L}}(\sqrt{r^2 + L^2})}\right) \mathcal{L}_{I_{\text{agg}}}^{\text{L}}\left(\frac{\gamma}{P\zeta_n^{\text{L}}(\sqrt{r^2 + L^2})}\right), \quad (14)$$

and

$$\Pr\left[\frac{P\zeta_n^{\text{NL}}(\sqrt{r^2 + L^2})h}{I_{\text{agg}} + P_{\text{N}}} > \gamma\right] = \exp\left(-\frac{\gamma P_{\text{N}}}{P\zeta_n^{\text{NL}}(\sqrt{r^2 + L^2})}\right) \mathcal{L}_{I_{\text{agg}}}^{\text{NL}}\left(\frac{\gamma}{P\zeta_n^{\text{NL}}(\sqrt{r^2 + L^2})}\right), \quad (15)$$

*Proof:* See Appendix A. ■

In Theorem 1,  $\mathcal{L}_{I_{\text{agg}}}^{\text{L}}(s)$  in (14) and  $\mathcal{L}_{I_{\text{agg}}}^{\text{NL}}(s)$  in (15) are the Laplace transform of  $I_{\text{agg}}$  evaluated at  $s$  for LoS signal transmission and that for NLoS transmission, respectively. For clarity, they are presented in the following Lemmas 2 and 3, respectively.

**Lemma 2.** In Theorem 1,  $\mathcal{L}_{I_{\text{agg}}}^{\text{L}}(s)$  is given by

$$\mathcal{L}_{I_{\text{agg}}}^{\text{L}}(s) = \exp\left(-2\pi\lambda \int_r^{+\infty} \frac{\Pr^{\text{L}}(\sqrt{u^2 + L^2}) u}{1 + (sP\zeta^{\text{L}}(\sqrt{u^2 + L^2}))^{-1}} du\right) \exp\left(-2\pi\lambda \int_{r_1}^{+\infty} \frac{[1 - \Pr^{\text{L}}(\sqrt{u^2 + L^2})] u}{1 + (sP\zeta^{\text{NL}}(\sqrt{u^2 + L^2}))^{-1}} du\right). \quad (16)$$

**Lemma 3.** In Theorem 1,  $\mathcal{L}_{I_{\text{agg}}}^{\text{NL}}(s)$  is given by

$$\mathcal{L}_{I_{\text{agg}}}^{\text{NL}}(s) = \exp\left(-2\pi\lambda \int_{r_2}^{+\infty} \frac{\text{Pr}^{\text{L}}(\sqrt{u^2 + L^2}) u}{1 + (sP\zeta^{\text{L}}(\sqrt{u^2 + L^2}))^{-1}} du\right) \exp\left(-2\pi\lambda \int_r^{+\infty} \frac{[1 - \text{Pr}^{\text{L}}(\sqrt{u^2 + L^2})] u}{1 + (sP\zeta^{\text{NL}}(\sqrt{u^2 + L^2}))^{-1}} du\right). \quad (17)$$

### B. The Area Spectral Efficiency

According to [9], [10], we also investigate the ASE in bps/Hz/km<sup>2</sup> for a given  $\lambda$ , which can be computed as

$$A^{\text{ASE}}(\lambda, \gamma_0) = \lambda \int_{\gamma_0}^{+\infty} \log_2(1 + \gamma) f_{\Gamma}(\lambda, \gamma) d\gamma, \quad (18)$$

where  $\gamma_0$  is the minimum working SINR for the considered SCN, and  $f_{\Gamma}(\lambda, \gamma)$  is the probability density function (PDF) of the SINR at the typical UE.

Based on the definition of  $p^{\text{cov}}(\lambda, \gamma)$  in (6), which is the complementary cumulative distribution function (CCDF) of SINR,  $f_{\Gamma}(\lambda, \gamma)$  can be expressed by

$$f_{\Gamma}(\lambda, \gamma) = \frac{\partial (1 - p^{\text{cov}}(\lambda, \gamma))}{\partial \gamma}, \quad (19)$$

where  $p^{\text{cov}}(\lambda, \gamma)$  is obtained from Theorem 1.

### C. The ASE Crash Theorem

Considering the results of  $p^{\text{cov}}(\lambda, \gamma)$  and  $A^{\text{ASE}}(\lambda, \gamma_0)$  respectively shown in (9) and (18), we propose Theorem 4 to theoretically explain the fundamental reasons of *the ASE Crash* discussed in Section I.

**Theorem 4.** *The ASE Crash Theorem: If  $L > 0$  and  $\gamma, \gamma_0 < +\infty$ , then  $\lim_{\lambda \rightarrow +\infty} p^{\text{cov}}(\lambda, \gamma) = 0$  and  $\lim_{\lambda \rightarrow +\infty} A^{\text{ASE}}(\lambda, \gamma_0) = 0$ .*

*Proof:* See Appendix B. ■

In essence, Theorem 4 states that when  $\lambda$  is extremely large, e.g., in UD SCNs, both  $p^{\text{cov}}(\lambda, \gamma)$  and  $A^{\text{ASE}}(\lambda, \gamma_0)$  will decrease towards zero with the network densification, and UEs will experience service outage, thus creating *the ASE Crash*. The fundamental reason for this phenomena is revealed by the key point of the proof, i.e., the signal power will lose its superiority over the interference power when  $\lambda \rightarrow +\infty$ , even if the interference created by the BSs that are relatively far away is ignored. This is because the absolute antenna height difference  $L$  introduces a *cap* on the signal-link distance and thus on the signal power. Although the interference power from each neighbouring cell is subject to the same cap,

the aggregate interference power will overwhelm the signal power in UD SCNs due to the sheer number of strong interferers growing from every direction around the interested UE. Theorem 4 is thus in stark contrast with the conclusion in [4], [7]–[10], which indicates that the increase in the interference power will be exactly counter-balanced by the increase in the signal power when  $\lambda \rightarrow +\infty$ .

Since the proof of Theorem 4 is mathematically intense and difficult to digest, in the following we provide a toy example to shed some valuable insights on the rationale behind the theorem. We consider a simple 2-BS SCN as illustrated in Fig. 2, where the 2D distance between the serving BS and the UE and that between an arbitrary interfering BS and the UE are denoted by  $r$  and  $\tau r$ , ( $1 < \tau < +\infty$ ), respectively.

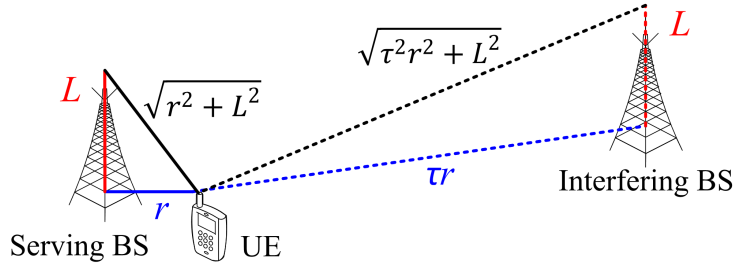


Fig. 2. Illustration of a toy example with a 2-BS SCN.

In this example,  $r \rightarrow 0$  when  $\lambda \rightarrow +\infty$ , which can be intuitively explained by the fact that the per-BS coverage area is roughly in the order of  $\frac{1}{\lambda}$ , and thus the typical 2D distance from the serving BS to the UE approaches zero when the BS density approaches infinity.

Considering that  $r \rightarrow 0$  and  $L$  is smaller than  $d_1$  in practical SCNs [5], [6], we can assume that both the signal link and the interference link should be dominantly characterized by *the first-piece LoS path loss function* in (3), i.e.,  $\zeta_1^L(w) = A_1^L (\sqrt{r^2 + L^2})^{-\alpha_1^L}$ . Thus, based on the 3D distances, we can obtain the signal-to-interference ratio (SIR)  $\bar{\gamma}$  as

$$\bar{\gamma} = \frac{A_1^L (\sqrt{r^2 + L^2})^{-\alpha_1^L}}{A_1^L (\sqrt{\tau^2 r^2 + L^2})^{-\alpha_1^L}} = \left( \sqrt{\frac{1}{1 + \frac{\tau^2 - 1}{1 + \frac{L^2}{r^2}}}} \right)^{-\alpha_1^L}. \quad (20)$$

Note that  $\bar{\gamma}$  monotonically decreases when  $\lambda$  increases or  $r$  decreases and  $L > 0$ . Moreover, it is easy to show that

$$\lim_{\lambda \rightarrow +\infty} \bar{\gamma} = \lim_{r \rightarrow 0} \bar{\gamma} = \begin{cases} 1, & (L > 0) \\ \tau^{\alpha_1^L}, & (L = 0) \end{cases}. \quad (21)$$

Assuming that  $\tau = 10$  and  $\alpha_1^L = 2$  in (21), the limit of  $\bar{\gamma}$  in UD SCNs will plunge from 20 dB when  $L = 0$  to 0 dB when  $L > 0$ , which means that even a rather weak interferer, e.g., with a power 20 dB below the signal power, will become a real threat to the signal link when the absolute antenna height difference  $L$  is non-zero in UD SCNs. For this example, Fig. 3 shows how  $\bar{\gamma}$  decreases when  $r$  decreases and  $L = 8.5$  m.

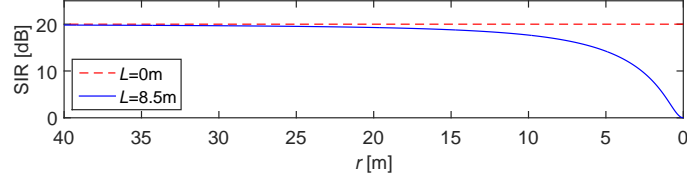


Figure 3.  $\bar{\gamma}$  vs.  $r$  when  $L = 8.5$  m,  $\tau = 10$  and  $\alpha_1^L = 2$ .

The drastic decrease of  $\bar{\gamma}$  when  $L > 0$  is due to *the cap imposed on the signal power* as the signal-link distance  $\sqrt{r^2 + L^2}$  in the numerator of (20) cannot go below  $L$ . Such cap on the signal-link distance and the signal power leads to *the ASE Crash*. This is because other signal-power-comparable interferers also approach the UE from all directions as  $\lambda$  increases, increasing the interference power, while the signal power remains constant. This will eventually cause service outage to the UE.

#### D. The 3GPP Special Cases

As a special case for Theorem 1, following [10], we consider a two-piece path loss and a linear LoS probability functions defined by the 3GPP [5], [6]. Specifically, we use the path loss function  $\zeta(w)$ , defined in the 3GPP as [5]

$$\zeta(w) = \begin{cases} A^L w^{-\alpha^L}, & \text{LoS: } \Pr^L(w) \\ A^{NL} w^{-\alpha^{NL}}, & \text{NLoS: } 1 - \Pr^L(w) \end{cases}, \quad (22)$$

together with a linear LoS probability function of  $\Pr^L(r)$ , defined in the 3GPP as [6]

$$\Pr^L(w) = \begin{cases} 1 - \frac{w}{d_1}, & 0 < w \leq d_1 \\ 0, & w > d_1 \end{cases}, \quad (23)$$

where  $d_1$  is a constant [6].

Considering the general path loss model presented in (2), the combined path loss model presented in (22) and (23) can be deemed as a special case of (2) with the following substitution:  $N = 2$ ,  $\zeta_1^L(w) = \zeta_2^L(w) = A^L w^{-\alpha^L}$ ,  $\zeta_1^{NL}(w) = \zeta_2^{NL}(w) = A^{NL} w^{-\alpha^{NL}}$ ,

$\Pr_1^L(w) = 1 - \frac{w}{d_1}$ , and  $\Pr_2^L(w) = 0$ . For clarity, this 3GPP special case is referred to as 3GPP Case 1 in the sequel. It should be noted that 3GPP Case 1 is compatible with the dense SCNs, because the exponential path loss function in [5] targets small cells and the LoS probability function in [6] also serves small cells only, which are referred to as microcells in [6].

To demonstrate that our conclusions have general significance, we consider another widely used LoS probability function, which is an exponential function defined in the 3GPP as [5]

$$\Pr^L(r) = \begin{cases} 1 - 5 \exp(-R_1/r), & 0 < r \leq d_1 \\ 5 \exp(-r/R_2), & r > d_1 \end{cases}, \quad (24)$$

where  $R_1$  and  $R_2$  are constants, and  $d_1 = \frac{R_1}{\ln 10}$ . The combination of the path loss function in (22) and the LoS probability function in (24) can then be deemed as a special case of the proposed path loss model in (2) with the following substitution:  $N = 2$ ,  $\zeta_1^L(r) = \zeta_2^L(r) = A^L r^{-\alpha^L}$ ,  $\zeta_1^{\text{NL}}(r) = \zeta_2^{\text{NL}}(r) = A^{\text{NL}} r^{-\alpha^{\text{NL}}}$ ,  $\Pr_1^L(r) = 1 - 5 \exp(-R_1/r)$ , and  $\Pr_2^L(r) = 5 \exp(-r/R_2)$ . For clarity, this combined case with both the path loss function and the LoS probability function coming from [5] is referred to as 3GPP Case 2 hereafter.

As justified in [10], we mainly use 3GPP Case 1 to generate the numerical results in Section V, because it provides tractable results for  $\{f_{R,n}^{\text{Path}}(r)\}$  and  $\{\mathcal{L}_{I_{\text{agg}}}^{\text{Path}}(s)\}$  in (10)-(17) of Theorem 1. The details are relegated to Appendix C. Nevertheless, we will numerically investigate 3GPP Case 2 using Theorem 1 in Section V, and we will show that similar conclusions like those for 3GPP Case 1 can also be drawn for 3GPP Case 2. More importantly, we will extend the analysis of 3GPP Case 1 (see Appendix C) to study an approximated 3GPP Case 2 in Section V, thus showing the usefulness of studying 3GPP Case 1 with the *linear* LoS probability function. To sum up, taking the linear LoS probability function from [6] to create 3GPP Case 1 not only allows us to obtain more tractable results but also prepares us to deal with more complicated path loss models.

Also note that eventually we may need to conduct hardware experiments in real-world fields to verify the existence of the ASE Crash. However, since there has been no ultra-dense network deployed in the world yet, it is difficult to do this at the current stage. Therefore, we use the propagation models that have been widely accepted by most industrial companies in the 3GPP [5], [6] to obtain the simulation results to verify our theoretical findings. Due to the limitation in using 3GPP Cases 1 and 2 to represent the real-world environment, the quantitative results in our study might deviate from those measured in practice, and thus we

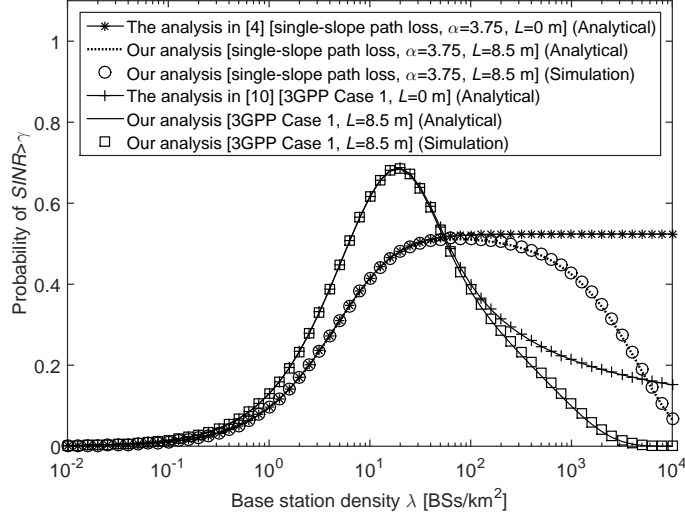


Fig. 4.  $p^{\text{cov}}(\lambda, \gamma)$  vs.  $\lambda$  with  $\gamma = 0$  dB.

should focus more on the qualitative conclusions of our theoretical discoveries.

## V. SIMULATION AND DISCUSSION

In this section, we investigate the network performance and use numerical results to establish the accuracy of our analysis. According to Tables A.1-3, A.1-4 and A.1-7 of [5] and [6], we adopt the following parameters for 3GPP Case 1:  $d_1 = 300$  m,  $\alpha^L = 2.09$ ,  $\alpha^{\text{NL}} = 3.75$ ,  $A^L = 10^{-10.38}$ ,  $A^{\text{NL}} = 10^{-14.54}$ ,  $P = 24$  dBm,  $P_N = -95$  dBm (including a noise figure of 9 dB at the UE). We have also investigated the results for a single-slope path loss model that does not differentiate LoS and NLoS transmissions [4], where only one path loss exponent  $\alpha$  is defined, the value of which is assumed to be  $\alpha = \alpha^{\text{NL}} = 3.75$ .

### A. Validation of Theorem 1 on the Coverage Probability

In Fig. 4, we show the results of  $p^{\text{cov}}(\lambda, \gamma)$  with  $\gamma = 0$  dB. Regarding the non-zero value of  $L$ , as explained in Section I, the BS antenna and the UE antenna heights are set to 10 m and 1.5 m, respectively [11], thus  $L = |10 - 1.5| = 8.5$  m.

As can be observed from Fig. 4, our analytical results given by Theorem 1 and Appendix C match the simulation results very well, which validates the accuracy of our analysis. From Fig. 4, we can draw the following observations, which confirm our discussion in Section I:

- For the single-slope path loss model with  $L = 0$  m, the BS density does NOT matter, since the coverage probability approaches a constant for UD SCNs [4], e.g.,  $\lambda > 10^2$  cells/km<sup>2</sup>.

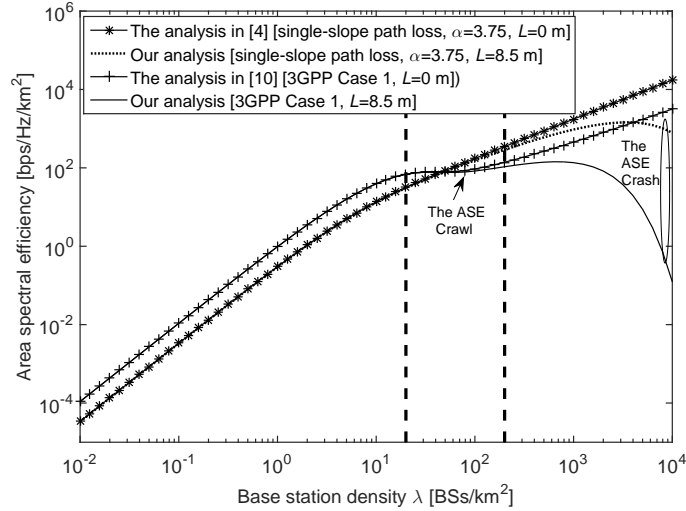


Fig. 5.  $A^{\text{ASE}}(\lambda, \gamma_0)$  vs.  $\lambda$  with  $\gamma_0 = 0$  dB.

- For the 3GPP Case 1 path loss model with  $L = 0$  m, *the BS density DOES matter*, since that coverage probability will decrease as  $\lambda$  increases when the network is dense enough, e.g.,  $\lambda > 20$  BSs/km<sup>2</sup>, due to the transition of a large number of interference paths from NLoS to LoS [10]. When  $\lambda$  is tremendously large, e.g.,  $\lambda \geq 10^3$  BSs/km<sup>2</sup>, the coverage probability decreases at a slower pace because both the interference and the signal powers are LoS dominated, and thus the coverage probability approaches a constant related to  $\alpha^L$  [4], [10].
- For both path loss models, when  $L = 8.5$  m, the coverage probability shows a determined trajectory toward zero in the UD SCN regime due to *the cap on the signal power* introduced by the non-zero  $L$  as explained in Theorem 4.

#### B. Validation of Theorem 4 on the ASE Crash

In Fig. 5, we show the results of  $A^{\text{ASE}}(\lambda, \gamma_0)$  with  $\gamma_0 = 0$  dB. Due to the significant accuracy of our analysis on  $p^{\text{cov}}(\lambda, \gamma)$  demonstrated in Fig. 4, we only show analytical results of  $A^{\text{ASE}}(\lambda, \gamma_0)$  in Fig. 5 and the following figures, because  $A^{\text{ASE}}(\lambda, \gamma_0)$  is computed from  $p^{\text{cov}}(\lambda, \gamma)$  as discussed in Subsection IV-B.

Fig. 5 is essentially the same as Fig. 1 with the same marker styles, except that the results for the single-slope path loss model with  $L = 8.5$  m are also plotted. From Fig. 5, we can confirm the key observations presented in Section I:

- For the single-slope path loss model with  $L = 0$  m, the ASE performance scales linearly with  $\lambda$  [4]. The result is promising, but it might not be the case in reality.



- For the 3GPP Case 1 path loss model with  $L = 0$  m, the ASE suffers from a slow growth or even a small *decrease* when  $\lambda \in [20, 200]$  BSs/km<sup>2</sup>, i.e., *the ASE Crawl* [10]. After *the ASE Crawl*, the ASE grows almost linearly again as the network further evolves to an UD SCN, e.g.,  $\lambda > 10^3$  BSs/km<sup>2</sup> [10].
- For both path loss models with  $L = 8.5$  m, the ASE suffers from severe performance loss in UD SCNs due to *the ASE Crash*, as explained in Theorem 4.

### C. The Performance Impact of $L$ on the ASE Crash

In Fig. 6, we show the results of  $A^{\text{ASE}}(\lambda, \gamma_0)$  with  $\gamma_0 = 0$  dB and various values of  $L$ . We assume that the UE antenna height is still 1.5 m, but the BS antenna height changes to 5 m, 10 m and 20 m, respectively. Accordingly,  $L$  takes the values of 3.5 m, 8.5 m and 18.5 m, respectively. Our key conclusions are summarized in the following:

- The larger the  $L$ , the severer *the ASE Crash*. In more detail, decreasing  $L$  from 18.5 m to 3.5 m helps to alleviate, but cannot remove *the ASE Crash* unless  $L = 0$ , as explained in Theorem 4. From Fig. 6, the ASE with  $L = 3.5$  m peaks at around  $\lambda^* = 3000$  BSs/km<sup>2</sup>, but it still suffers from a 60 % loss compared with that with  $L = 0$  m at  $\lambda^*$ .
- As far as we know, the BS antenna height has never gone below 6 m in current deployments. In the future, we foresee two possibilities. (1) The BS antenna height will indeed go very low and that would be a desirable thing according to our study. However, such deployment opens new R&D challenges, which are to be discussed in Subsection V-G. (2) The BS antenna height will go lower but never below, say 5 m, to take advantage of the current infrastructure or street furniture. Then our study would provide an interesting prediction about the ASE Crash when the network is sufficiently dense. For either possibility, our study would be useful, shedding new light on the dense SCN deployment.

### D. The Performance Impact of $\alpha^L$ and Rician Fading on the ASE Crash

In Fig. 7, we investigate the performance of  $A^{\text{ASE}}(\lambda, \gamma_0)$  under the assumptions of  $\alpha^L = 1.09$  [10] or Rician fading [6]. Here we adopt a practical model of Rician fading in [6], where the  $K$  factor in dB scale (the ratio between the power in the direct path and the power in the other scattered paths) is modeled as  $K[\text{dB}] = 13 - 0.03w$ , where  $w$  is the 3D distance in meter. Note that Theorem 4 is derived for Rayleigh fading only, and it is challenging to

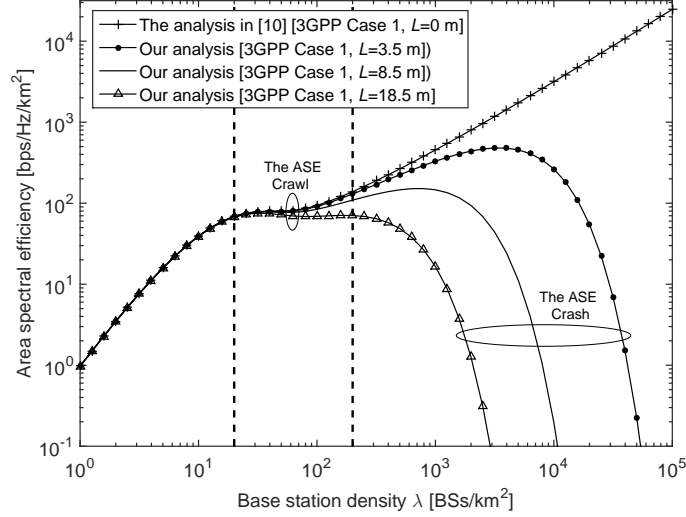


Fig. 6.  $A^{\text{ASE}}(\lambda, \gamma_0)$  vs.  $\lambda$  with  $\gamma_0 = 0$  dB and various  $L$ .

obtain analytical results for Rician fading. Therefore, we only display simulation results for Rician fading in Fig. 7 and leave the related theoretical analysis as our future work. Our key conclusions from Fig. 7 are summarized as follows:

- Decreasing  $\alpha^L$  helps to alleviate *the ASE Crash* because it softens the SIR crash in (21). However, it aggravates *the ASE Crawl* by showing an obvious ASE decrease when  $\lambda \in [20, 80]$  BSs/km<sup>2</sup> due to the more drastic interference transition from NLoS to stronger LoS of  $\alpha^L=1.09$  compared with  $\alpha^L=2.09$  defined in 3GPP Case 1 [10].
- From the simulation results, we can see that Rician fading makes *the ASE Crash* worse, which takes effect earlier than the case with Rayleigh fading. The intuition is that the randomness in channel fluctuation associated with Rician fading is much weaker than that associated with Rayleigh fading due to the large  $K$  factor in UD SCNs [6]. With Rayleigh fading, some UE in outage might be opportunistically saved by favorable channel fluctuation of the signal power, while with Rician fading, such outage case becomes more deterministic due to lack of channel variation, thus leading to a severer *ASE Crash*.
- It is important to note that the impact of Rayleigh and Rician fading on the ASE Crawl is minor [10]. This is because the ASE Crawl is caused by the transition of a large number of interference paths from NLoS to LoS with the network densification. The strength of the NLoS to LoS transition is in the order of 10dB~20dB according to the 3GPP path loss functions. Hence, Rayleigh or Rician fading makes little difference against this

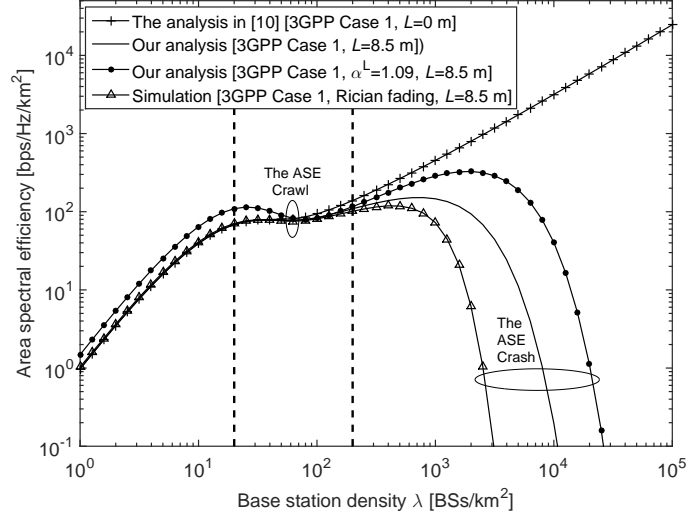


Fig. 7.  $A^{\text{ASE}}(\lambda, \gamma_0)$  vs.  $\lambda$  with  $\gamma_0 = 0$  dB and assumptions of  $\alpha^L = 1.09$  or Rician fading.

abrupt change of interference strength.

#### E. The Performance Impact of Antenna Pattern and Downtilt on the ASE Crash

As discussed in Section III, via downtilt in the vertical domain, a practical antenna can target its antenna beam towards a given direction, which may affect *the ASE Crash* behavior. Here we adopt the antenna pattern and downtilt model proposed in [21]. More specifically, in our analysis, the path loss function  $\zeta(w)$  in (2) should be replaced by  $\zeta(w) 10^{\frac{1}{10}G(\varphi, \theta, \theta_{\text{tilt}})}$ , where  $G(\varphi, \theta, \theta_{\text{tilt}})$  is the antenna gain in the dB unit and it can be expressed by

$$G(\varphi, \theta, \theta_{\text{tilt}}) = G_{\text{M}} + G_{\text{H}}(\varphi) + G_{\text{V}}(\theta, \theta_{\text{tilt}}), \quad (25)$$

where  $\varphi$  and  $\theta$  are the angles of arrival in the horizontal and vertical planes, respectively,  $\theta_{\text{tilt}}$  is the electrical downtilt angle of the vertical antenna beam,  $G_{\text{M}}$  is the maximum antenna gain in dB,  $G_{\text{H}}(\varphi)$  is the horizontal attenuation offset in dB, and  $G_{\text{V}}(\theta, \theta_{\text{tilt}})$  is the vertical attenuation offset in dB.

Considering a 4-element half-wave dipole antenna, we have  $G_{\text{M}} = 8.15$  dB [21]. For the horizontal pattern, as discussed in Section III, we consider a omni-directional antenna, i.e.,  $G_{\text{H}}(\varphi) = 0$  dB. For the vertical pattern,  $G_{\text{V}}(\theta, \theta_{\text{tilt}})$  is formulated according to [21] as

$$G_{\text{V}}(\theta, \theta_{\text{tilt}}) = \max \{10 \log_{10} |\cos^n(\theta - \theta_{\text{tilt}})|, F_{\text{V}}\}, \quad (26)$$

where  $n$  equals to 47.64 for a 4-element half-wave dipole antenna with a vertical half-power

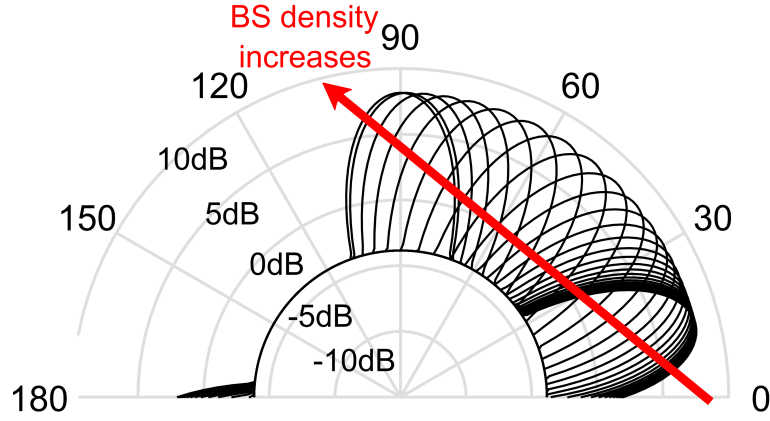


Fig. 8.  $G(\varphi, \theta, \theta_{\text{tilt}})$  vs.  $\theta$  for a 4-element half-wave dipole antenna [21], [22].

band-width (HPBW) of  $B_V = 19.5$  degrees, and  $F_V$  is the vertical side-lobe level (SLL), which is set to -12 dB in [21]. As discussed in Section III, it is important to note that in practice  $\theta_{\text{tilt}}$  becomes larger as the BS density  $\lambda$  increases. According to [22],  $\theta_{\text{tilt}}$  can be empirically modeled as

$$\theta_{\text{tilt}} = \arctan\left(\frac{L}{r^{\text{cov}}}\right) + zB_V, \quad (27)$$

where  $r^{\text{cov}}$  is the average distance from a cell-edge UE to its serving BS given by  $r^{\text{cov}} = \sqrt{\frac{1}{\lambda\pi}}$  in our analysis, and  $z$  is an empirical parameter achieving a good trade-off between the received signal power and the resulting inter-cell interference. In [22],  $z$  is set to 0.7.

Plugging (27) into (26), we can obtain the antenna gain  $G(\varphi, \theta, \theta_{\text{tilt}})$  considering practical antenna pattern and downtilt. Such results are illustrated in Fig. 8. From this figure, we can observe that the downtilt angle of the vertical antenna beam gradually increases from around 10 degrees to 90 degrees as the network densifies, and the maximum antenna gain is  $G_M = 8.15$  dB at the direction of such downtilt angle.

Based on the results of  $G(\varphi, \theta, \theta_{\text{tilt}})$  displayed in Fig. 8, we investigate the performance of  $A^{\text{ASE}}(\lambda, \gamma_0)$  with practical antenna pattern and downtilt in Fig. 9. Our key conclusion from Fig. 9 is drawn as follows:

- The practical antenna pattern and downtilt shown in Fig. 8 help to alleviate *the ASE Crash* because they constrain the BS energy emission within certain geometrical areas. However, *the ASE Crash* still emerges in UD SCNs because the cap on the signal power persists, even if the BS antenna faces downward with a downtilt angle of 90 degrees.

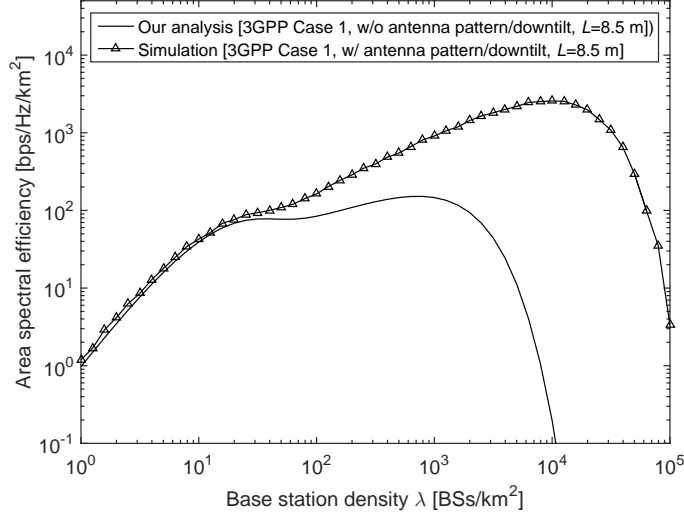


Fig. 9.  $A^{\text{ASE}}(\lambda, \gamma_0)$  vs.  $\lambda$  with  $\gamma_0 = 0$  dB and the practical antenna pattern and downtilt shown in Fig. 8.

#### F. The Performance Impact of 3GPP Case 2 on the ASE Crash

In this subsection, we investigate the ASE performance for 3GPP Case 2, which has been discussed in Subsection IV-D. The parameters in the LoS probability function  $\text{Pr}^{\text{L}}(r)$  of 3GPP Case 2 are set to  $R_1 = 156$  m and  $R_2 = 30$  m [5]. First, we directly apply the numerical integration in Theorem 1 to evaluate the ASE result for 3GPP Case 2. Second, in order to show the versatility of the studied 3GPP Case 1 with the *linear* LoS probability function shown in (23), as in [10], we adopt the technique of approximating the LoS probability function of 3GPP Case 2 shown in (24) by a 3-piece *linear* function as

$$\text{Pr}^{\text{L}}(r) = \begin{cases} 1, & 0 < r \leq d_1 \\ 1 - \frac{r-d_1}{d_2-d_1}, & d_1 < r \leq d_2 \\ 0, & r > d_2 \end{cases}, \quad (28)$$

where  $d_1$  and  $d_2$  are set to 18.4 m and 117.1 m, respectively. Note that the approximation of (28) can be easily improved by fitting the LoS probability function with more than three pieces in (28). For clarity, the combined case with the path loss function of (22) and the 3-piece LoS probability function of (28) is referred to as the Approximated 3GPP Case 2. Based on Theorem 1, we can readily extend the results in Appendix C to analyze the Approximated 3GPP Case 2 in a tractable manner. The details are very similar to those in [10] and thus omitted here for brevity.

In Fig. 10, we show the results of  $A^{\text{ASE}}(\lambda, \gamma_0)$  for 3GPP Case 2. As can be seen from Fig. 10, the results of the Approximated 3GPP Case 2 based on (28) match those of 3GPP

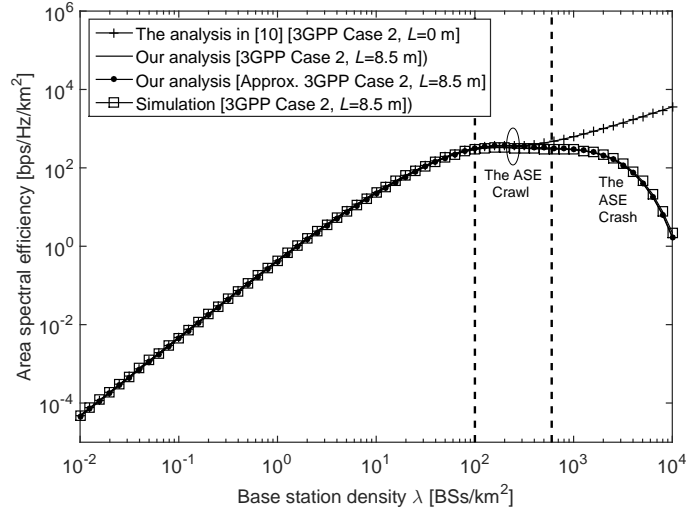


Fig. 10.  $A^{\text{ASE}}(\lambda, \gamma_0)$  vs.  $\lambda$  with  $\gamma_0 = 0$  dB for 3GPP Case 2.

Case 2 very well for a wide range of  $\lambda$ , thus showing the extensibility of our analysis with the *linear* LoS probability function. More importantly, all the observations in Subsection V-B are qualitatively valid for Fig. 10 except for some quantitative deviation. In more detail,

- The BS density range of *the ASE Crawl* for 3GPP Case 2 is around  $\lambda \in [200, 600]$  BSs/km<sup>2</sup>.
- For 3GPP Case 2 with  $L = 8.5$  m, the ASE also suffers from severe performance loss in UD SCNs, e.g.,  $\lambda > 10^3$  BSs/km<sup>2</sup>, due to *the ASE Crash*, as explained in Theorem 4.

#### G. A Novel BS Deployment with UE-Height Antennas

Based on our thought-provoking discovery, we make the following recommendation to vendors and operators around the world: The BS antenna height should be lowered to the UE antenna height in 5G UD SCNs, so that the ASE behavior of such networks would roll back to our previous results in [9], [10], thus avoiding *the ASE Crash*. Such proposed new BS deployment will allow to realize the potential gains of UD SCNs, but needs a revolution on BS architectures and network deployment in 5G. The new R&D challenges in this area are:

- 1) Measurement campaigns for the UE-height channels, which will be used to confirm the existence of the ASE Crash in more practical environments.
- 2) Terrain-dependent network performance analysis considering bridges, hills, elevated roads, etc.

- 3) New BS architectures/hardware that are anti-vandalism/anti-theft/anti-hacking at low-height positions.

## VI. CONCLUSION

We presented a new and significant theoretical discovery, i.e., the serious problem of *the ASE Crash*. If the absolute height difference between BS antenna and UE antenna is larger than zero, then the ASE performance will continuously decrease toward with the network densification for UD SCNs. One way to overcome *the ASE Crash* is to lower the SCN BS antenna height to the UE antenna height, which will revolutionize the approach of BS architecture and deployment in 5G. Other ways to counter-measure *the ASE Crash* could be pro-active muting of BSs, dynamic beam tracking, cooperation of neighbouring BSs, etc., which are worth further studying in the context of UDNs. Also, it is worthwhile to conduct a comparison study on the intensity matching approach [15] and our analysis in terms of the accuracy loss due to approximation and the computational complexity, etc.

### APPENDIX A: PROOF OF THEOREM 1

For clarity, we first summarize our ideas to prove Theorem 1. In order to evaluate  $p^{\text{cov}}(\lambda, \gamma)$ , we need to calculate the coverage probability components  $T_n^{\text{L}}$  and  $T_n^{\text{NL}}$ , for the cases when the signal comes from the  $n$ -th piece LoS path (denoted by Event  $B_n^{\text{L}}$ ) and when the signal comes from the  $n$ -th piece NLoS path (denoted by Event  $B_n^{\text{NL}}$ ), respectively. Then, to calculate  $T_n^{\text{L}}$ , we need to know two things so that we can perform an integral with respect to the 2D signal-link distance  $r$  to obtain  $T_n^{\text{L}}$ , i.e., (i) the joint PDF of  $r$  and Event  $B_n^{\text{L}}$ , denoted by  $f_{R,n}^{\text{L}}(r)$ , and (ii) the coverage probability conditioned on  $(r, B_n^{\text{L}})$ , i.e.,  $\Pr[\text{SINR} > \gamma | (r, B_n^{\text{L}})]$ . Note that the derivation of  $T_n^{\text{NL}}$  is similar to that of  $T_n^{\text{L}}$ .

From (6), (7) and the definition of  $w$  in (1), we can derive  $p^{\text{cov}}(\lambda, \gamma)$  as

$$\begin{aligned}
 p^{\text{cov}}(\lambda, \gamma) &\stackrel{(a)}{=} \int_{r>0} \Pr[\text{SINR} > \gamma | r] f_R(r) dr \\
 &= \sum_{n=1}^N \int_{\sqrt{d_{n-1}^2 - L^2}}^{\sqrt{d_n^2 - L^2}} \Pr[\text{SINR} > \gamma | (r, B_n^{\text{L}})] f_{R,n}^{\text{L}}(r) dr \\
 &\quad + \sum_{n=1}^N \int_{\sqrt{d_{n-1}^2 - L^2}}^{\sqrt{d_n^2 - L^2}} \Pr[\text{SINR} > \gamma | (r, B_n^{\text{NL}})] f_{R,n}^{\text{NL}}(r) dr \\
 &\triangleq \sum_{n=1}^N (T_n^{\text{L}} + T_n^{\text{NL}}), \tag{29}
 \end{aligned}$$



where  $f_{R,n}^{Path}(r)$  is the joint PDF of  $r$  and Event  $B_n^{Path}$ , where the string variable  $Path$  takes the value of “L” and “NL” for the LoS and the NLoS cases, respectively. Note that  $f_{R,n}^{Path}(r)$  should satisfy the following normalization condition,

$$\sum_{n=1}^N \int_{\sqrt{d_{n-1}^2 - L^2}}^{\sqrt{d_n^2 - L^2}} f_{R,n}^L(r) dr + \sum_{n=1}^N \int_{\sqrt{d_{n-1}^2 - L^2}}^{\sqrt{d_n^2 - L^2}} f_{R,n}^{NL}(r) dr = 1. \quad (30)$$

The two events  $B_n^L$  and  $B_n^{NL}$  are disjoint events. Hence, the coverage probability is the sum of two probabilities, which correspond to those two disjoint events, respectively. Moreover, in (29),  $T_n^L$  and  $T_n^{NL}$  are piece-wise functions defined in (9), and  $d_0$  and  $d_N$  are respectively defined as  $L$  and  $+\infty$ .

In the following, we discuss how to obtain  $f_{R,n}^L(r)$  and  $f_{R,n}^{NL}(r)$ .

By definition,  $f_{R,n}^L(r)$  should be calculated as  $f_{R,n|B_n^L}(r|B_n^L) \Pr[B_n^L]$ , where  $\Pr[B_n^L] = \Pr_n^L(\sqrt{r^2 + L^2})$  according to (3) and  $f_{R,n|B_n^L}(r|B_n^L)$  should characterize the joint event of the following three independent sub-events:

- 1) For the typical UE, its serving BS  $b_o$  should exist at the 2D distance  $r$  from it and the corresponding unconditional PDF of  $r$  is  $2\pi r\lambda$  [4].
- 2) There should be no LoS BS that can provide a better link to the typical UE than the LoS BS  $b_o$  in Event  $B_n^L$  [10], the probability of which is

$$p_n^L(r) = \exp\left(-\int_0^r \Pr^L(\sqrt{u^2 + L^2}) 2\pi u \lambda du\right). \quad (31)$$

- 3) There should be no NLoS BS that can provide a better link to the typical UE than the LoS BS  $b_o$  in Event  $B_n^L$  [10], the probability of which is

$$p_n^{NL}(r) = \exp\left(-\int_0^{r_1} \left(1 - \Pr^L(\sqrt{u^2 + L^2})\right) 2\pi u \lambda du\right), \quad (32)$$

where  $r_1$  is computed by (12) to find the 2D distance at which a NLoS BS has the same signal reception level as  $b_o$ .

Similar to [10] and with special attention paid to the 3D distances, it is easy to show that

$$f_{R,n|B_n^L}(r|B_n^L) = p_n^{NL}(r) p_n^L(r) 2\pi r \lambda. \quad (33)$$

Thus,  $f_{R,n}^L(r)$  can be written as (10). In a similar way, we can obtain  $f_{R,n}^{NL}(r)$  from (11).

Next, we discuss how to derive  $\Pr[\text{SINR} > \gamma | (r, B_n^L)]$  and  $\Pr[\text{SINR} > \gamma | (r, B_n^{NL})]$ .

Regarding  $\Pr[\text{SINR} > \gamma | (r, B_n^L)]$ , it can be expressed as  $\Pr\left[\frac{P\zeta_n^L(\sqrt{r^2 + L^2})h}{I_{\text{agg}} + P_N} > \gamma\right]$  in (29)

and calculated as

$$\begin{aligned} \Pr \left[ \frac{P\zeta_n^L(\sqrt{r^2+L^2})h}{I_{\text{agg}}+P_N} > \gamma \right] &= \mathbb{E}_{[I_{\text{agg}}]} \left\{ \Pr \left[ h > \frac{\gamma(I_{\text{agg}}+P_N)}{P\zeta_n^L(\sqrt{r^2+L^2})} \right] \right\} \\ &= \mathbb{E}_{[I_{\text{agg}}]} \left\{ \bar{F}_H \left( \frac{\gamma(I_{\text{agg}}+P_N)}{P\zeta_n^L(\sqrt{r^2+L^2})} \right) \right\}, \end{aligned} \quad (34)$$

where  $\mathbb{E}_{[X]} \{\cdot\}$  denotes the expectation operation taking the expectation over the variable  $X$  and  $\bar{F}_H(h)$  denotes the CCDF of RV  $h$ . Since we assume  $h$  to be an exponential RV, we have  $\bar{F}_H(h) = \exp(-h)$  and thus (34) can be further derived as

$$\begin{aligned} \Pr \left[ \frac{P\zeta_n^L(\sqrt{r^2+L^2})h}{I_{\text{agg}}+P_N} > \gamma \right] &= \mathbb{E}_{[I_{\text{agg}}]} \left\{ \bar{F}_H \left( \frac{\gamma(I_{\text{agg}}+P_N)}{P\zeta_n^L(\sqrt{r^2+L^2})} \right) \right\} \\ &= \exp \left( -\frac{\gamma P_N}{P\zeta_n^L(\sqrt{r^2+L^2})} \right) \mathbb{E}_{[I_{\text{agg}}]} \left\{ \exp \left( -\frac{\gamma I_{\text{agg}}}{P\zeta_n^L(\sqrt{r^2+L^2})} \right) \right\} \\ &= \exp \left( -\frac{\gamma P_N}{P\zeta_n^L(\sqrt{r^2+L^2})} \right) \mathcal{L}_{I_{\text{agg}}}^L \left( \frac{\gamma}{P\zeta_n^L(\sqrt{r^2+L^2})} \right), \end{aligned} \quad (35)$$

where  $\mathcal{L}_{I_{\text{agg}}}^L(s)$  is the Laplace transform of RV  $I_{\text{agg}}$  evaluated at  $s$  on the condition of Event  $B^L$  that the typical UE is associated with a BS with a LoS path. Based on the presented UAS, we can derive  $\mathcal{L}_{I_{\text{agg}}}^L(s)$  as

$$\begin{aligned} \mathcal{L}_{I_{\text{agg}}}^L(s) &= \mathbb{E}_{[I_{\text{agg}}]} \left\{ \exp(-sI_{\text{agg}}) | B^L \right\} \\ &= \mathbb{E}_{[\Phi, \{\beta_i\}, \{g_i\}]} \left\{ \exp \left( -s \sum_{i \in \Phi/b_o} P\beta_i(w)g_i \right) \middle| B^L \right\}. \end{aligned} \quad (36)$$

According to [4],  $\mathbb{E}_{[g]} \left\{ \exp(-sP\beta(w)g) | B^L \right\}$  in (36) should consider interference from both LoS and NLoS paths. Thus,  $\mathcal{L}_{I_{\text{agg}}}^L(s)$  can be further derived as

$$\begin{aligned} \mathcal{L}_{I_{\text{agg}}}^L(s) &= \exp \left( -2\pi\lambda \int_r^{+\infty} \text{Pr}^L(\sqrt{u^2+L^2}) \left[ 1 - \mathbb{E}_{[g]} \left\{ \exp \left( -sP\zeta^L(\sqrt{u^2+L^2})g \right) \right\} \right] u du \right. \\ &\quad \left. - 2\pi\lambda \int_{r_1}^{+\infty} \left[ 1 - \text{Pr}^L(\sqrt{u^2+L^2}) \right] \left[ 1 - \mathbb{E}_{[g]} \left\{ \exp \left( -sP\zeta^{\text{NL}}(\sqrt{u^2+L^2})g \right) \right\} \right] u du \right) \\ &= \exp \left( -2\pi\lambda \int_r^{+\infty} \frac{\text{Pr}^L(\sqrt{u^2+L^2})u}{1+(sP\zeta^L(\sqrt{u^2+L^2}))^{-1}} du \right) \exp \left( -2\pi\lambda \int_{r_1}^{+\infty} \frac{[1-\text{Pr}^L(\sqrt{u^2+L^2})]u}{1+(sP\zeta^{\text{NL}}(\sqrt{u^2+L^2}))^{-1}} du \right). \end{aligned} \quad (37)$$

Plugging  $s = \frac{\gamma}{P\zeta_n^L(\sqrt{r^2+L^2})}$  into (37) and further plugging (37) into (35), we can obtain the general expression of  $\Pr \left[ \frac{P\zeta_n^L(\sqrt{r^2+L^2})h}{I_{\text{agg}}+P_N} > \gamma \right]$  shown in (14). Note that in (14),

- $\exp \left( -\frac{\gamma P_N}{P\zeta_n^L(\sqrt{r^2+L^2})} \right)$  is the probability that *the signal power beats the noise power* by a factor of at least  $\gamma$ .
- $\mathcal{L}_{I_{\text{agg}}}^L \left( \frac{\gamma}{P\zeta_n^L(\sqrt{r^2+L^2})} \right)$  is the probability that *the signal power beats the aggregate interference power* by a factor of at least  $\gamma$ . Specifically, in the expression of  $\mathcal{L}_{I_{\text{agg}}}^L(s)$  given by (16), the first (second) term of the product calculates the probability that the signal power beats the aggregate interference power from all LoS (NLoS) BSs by a factor of at least  $\gamma$ .
- Considering the assumption that  $h$  follows an exponential distribution, we can invoke  $\Pr[h > \gamma(a+b)] = \Pr[h > \gamma a] \Pr[h > \gamma b]$ ,  $(a, b \in \mathbb{R}^+)$ , and thus the product of the two probabilities in the above bulletins yields the probability that *the signal power beats the sum power of the noise and the aggregate interference* by a factor of at least  $\gamma$ .

In a similar way, we can obtain the general expression of  $\Pr \left[ \frac{P\zeta_n^{\text{NL}}(\sqrt{r^2+L^2})h}{I_{\text{agg}}+P_N} > \gamma \right]$  shown in (15). Our proof of Theorem 1 is completed by plugging (10), (14), (11) and (15) into (29).

## APPENDIX B: PROOF OF THEOREM 4

By applying the theory of limits on  $p^{\text{cov}}(\lambda, \gamma)$  derived in Theorem 1, we can obtain that

$$\lim_{\lambda \rightarrow +\infty} p^{\text{cov}}(\lambda, \gamma) = \lim_{\lambda \rightarrow +\infty} T_1^L + \lim_{\lambda \rightarrow +\infty} T_1^{\text{NL}}. \text{ This is because}$$

- When  $\lambda \rightarrow +\infty$ , the typical 2D distance  $r$  from the UE to its serving BS  $b_o$  approaches zero, i.e.,  $r \rightarrow 0$ , which should be dominantly characterized by either *the first-piece LoS path loss function* or *the first-piece NLoS path loss function* due to the short-distance link and  $L$  is smaller than  $d_1$  in practical SCNs [5], [6]; and
- According to Appendix A,  $T_1^L$  and  $T_1^{\text{NL}}$  measure nothing but the components of the coverage probability for the cases that the signal comes from *the first-piece LoS path* and that the signal comes from *the first-piece NLoS path*, respectively.

Moreover, when  $\lambda \rightarrow +\infty$ , we have  $\lim_{\lambda \rightarrow +\infty} T_1^{\text{NL}} = 0$  due to  $\lim_{\lambda \rightarrow +\infty} f_{R,1}^{\text{NL}}(r) = 0$ . In more detail,  $f_{R,1}^{\text{NL}}(r)$  approaches zero when  $\lambda \rightarrow +\infty$ , i.e.,  $r \rightarrow 0$ , because

- According to (13),  $\lim_{r \rightarrow 0} r_2 = \arg \left\{ \zeta^L \left( \sqrt{r_2^2 + L^2} \right) = \zeta_1^{\text{NL}}(L) \right\} \triangleq r_2^{\min}$ , which is a non-zero value due to the non-zero value of  $L$ .

- Thus, the term  $\exp\left(-\int_0^{r_2} \Pr^L\left(\sqrt{u^2 + L^2}\right) 2\pi u \lambda du\right)$  in (11) can be upper-bounded by  $\exp\left(-\int_0^{r_2} \Pr^L\left(\sqrt{u^2 + L^2}\right) 2\pi u \lambda du\right) \leq \exp\left(-\Pr^L\left(\sqrt{(r_2^{\min})^2 + L^2}\right) \pi \lambda (r_2^{\min})^2\right)$ ,

which approaches zero when  $\lambda \rightarrow +\infty$ . Note that we assume  $\Pr^L(w)$  to be a monotonically decreasing function with respect to  $w$  as explained in Section III.

- Hence, we can obtain  $\lim_{\lambda \rightarrow +\infty} f_{R,1}^{\text{NL}}(r) = 0$  considering the definition of  $f_{R,1}^{\text{NL}}(r)$  in (11).

Therefore, we can claim that  $\lim_{\lambda \rightarrow +\infty} p^{\text{cov}}(\lambda, \gamma) = \lim_{\lambda \rightarrow +\infty} T_1^L$ , which is in line with the intuitive fact that when  $\lambda \rightarrow +\infty$ , the coverage probability should be mainly contributed by the case that the signal comes from *the first-piece LoS path*.

Next, we show that  $\lim_{\lambda \rightarrow +\infty} \Pr\left[\frac{P\zeta_1^L(\sqrt{r^2+L^2})h}{I_{\text{agg}}+N_0} > \gamma\right] = 0$ , so that we can get  $\lim_{\lambda \rightarrow +\infty} T_1^L = 0$ .

From (14) and (16), we have

$$\Pr\left[\frac{P\zeta_1^L(\sqrt{r^2+L^2})h}{I_{\text{agg}}+N_0} > \gamma\right] < \exp\left(-2\pi\lambda \int_r^{+\infty} \frac{\Pr^L(\sqrt{u^2+L^2})u}{1 + \left(\frac{\gamma P\zeta_1^L(\sqrt{u^2+L^2})}{P\zeta_1^L(\sqrt{r^2+L^2})}\right)^{-1}} du\right) \quad (38)$$

$$< \exp\left(-2\pi\lambda \int_r^{\tau r} \frac{\Pr^L(\sqrt{u^2+L^2})u}{1 + \frac{1}{\gamma} \left(\frac{\sqrt{r^2+L^2}}{\sqrt{u^2+L^2}}\right)^{-\alpha_1^L}} du\right) \quad (39)$$

$$< \exp\left(-2\pi\lambda \frac{\Pr^L(\sqrt{\tau^2 r^2 + L^2}) \int_r^{\tau r} u du}{1 + \frac{1}{\gamma} \left(\frac{\sqrt{r^2+L^2}}{\sqrt{\tau^2 r^2 + L^2}}\right)^{-\alpha_1^L}}\right) \quad (40)$$

$$\stackrel{r \rightarrow 0}{\leq} \exp\left(-\frac{\Pr^L(L)(\tau^2 - 1)}{1 + \frac{1}{\gamma}}\right) \triangleq \kappa, \quad (41)$$

where  $\kappa$  is derived because

- As explained in Appendix A, (38) only considers the probability that the signal power beats the aggregate interference power from all LoS BSs by a factor of at least  $\gamma$ , which over-estimates the coverage probability. Besides,  $s = \frac{\gamma}{P\zeta_1^L(\sqrt{r^2+L^2})}$  is plugged into (38).
- In (39), we further concentrate on the LoS interference that is relatively close to the UE, i.e.,  $u \in (r, \tau r]$ , ( $1 < \tau < +\infty$ ). Besides, *the first-piece LoS path loss function* has also been used for such LoS interference, because when  $r \rightarrow 0$  we have  $\tau r \rightarrow 0$ , which falls into the region that is dominantly characterized by *the first-piece LoS path loss function*.
- We arrive at (40) because (i)  $\left(\frac{\sqrt{r^2+L^2}}{\sqrt{u^2+L^2}}\right)^{-\alpha_1^L} < \left(\frac{\sqrt{r^2+L^2}}{\sqrt{\tau^2 r^2 + L^2}}\right)^{-\alpha_1^L}$ ,  $u \in (r, \tau r]$ ; and (ii)  $\Pr^L(\sqrt{u^2+L^2}) > \Pr^L(\sqrt{\tau^2 r^2 + L^2})$ ,  $u \in (r, \tau r]$ , since  $\Pr^L(w)$  is a monotonically

decreasing function with respect to  $w$  as explained in Section III.

- Finally, we plug  $\lim_{\lambda \rightarrow +\infty} \Pr^L(\sqrt{\tau^2 r^2 + L^2}) = \Pr^L(L)$ ,  $\lim_{\lambda \rightarrow +\infty} \frac{\sqrt{r^2 + L^2}}{\sqrt{\tau^2 r^2 + L^2}} = 1$ ,  $\int_r^{\tau r} u du = \frac{1}{2}(\tau^2 - 1)r^2$  and  $\lim_{\lambda \rightarrow +\infty} \pi r^2 \lambda = 1$  into (40) to obtain (41). Note that we have  $\lim_{\lambda \rightarrow +\infty} \pi r^2 \lambda = 1$  because the typical coverage radius, denoted by  $\hat{r}$ , permits  $\lim_{\lambda \rightarrow +\infty} \pi \hat{r}^2 \lambda = 1$  (the typical coverage area  $\pi \hat{r}^2$  is in the order of  $\frac{1}{\lambda}$ ). Hence,  $\lim_{\lambda \rightarrow +\infty} \pi r^2 \lambda = 1$  holds because  $r \rightarrow \hat{r}$  when  $\lambda \rightarrow +\infty$ .

Since  $\tau$  takes an arbitrary and finite value, we have  $\lim_{\lambda \rightarrow +\infty} \Pr \left[ \frac{P\zeta_1^L(\sqrt{r^2 + L^2})h}{I_{\text{agg}} + N_0} > \gamma \right] = 0$  because  $\kappa$  can be reduced to any arbitrarily small value when  $\tau$  is sufficiently large. For example, when  $\Pr^L(L) = 0.8$ ,  $\gamma = 1$ , and  $\tau$  equals to a moderate value of 8, then  $\kappa$  is smaller than  $1 \times 10^{-11}$ . Therefore, according to the definition of  $T_1^L$  in (9), we can get  $\lim_{\lambda \rightarrow +\infty} T_1^L = \lim_{\lambda \rightarrow +\infty} p^{\text{cov}}(\lambda, \gamma) = 0$ .

Furthermore, since  $\gamma$  is arbitrary for  $p^{\text{cov}}(\lambda, \gamma)$ , we can set  $\gamma > \gamma_0$  and put the UE into a complete outage in UD SCNs, i.e.,  $\lim_{\lambda \rightarrow +\infty} \Pr[\text{SINR} > \gamma_0] \equiv 0$ . Since the UD SCNs are now operating below the minimum working SINR  $\gamma_0$ , according to the definition of ASE in (18), we have  $\lim_{\lambda \rightarrow +\infty} A^{\text{ASE}}(\lambda, \gamma_0) = 0$ , which completes our proof.

### APPENDIX C: SPECIAL CASE STUDY ON 3GPP CASE 1

For 3GPP Case 1, according to Theorem 1,  $p^{\text{cov}}(\lambda, \gamma)$  can be computed by plugging (22) and (23) into (10)-(17). In order to increase the tractability of the results, we propose the following approximation for  $w = \sqrt{r^2 + L^2}$  in (10)-(17),

$$w \approx \tilde{w} = \begin{cases} L, & 0 \leq r \leq v_1 \\ \frac{r+L}{\sqrt{2}}, & v_1 \leq r \leq v_2 \\ r, & r > v_2 \end{cases}, \quad (42)$$

where  $v_1 = (\sqrt{2} - 1)L$  and  $v_2 = (\sqrt{2} + 1)L$ . Such approximation is based on the following three lower bounds of  $w$ :

- $w = \sqrt{r^2 + L^2} \geq L$ , which is tight when  $r$  is very small, i.e.,  $0 \leq r \leq v_1$ .
- $w = \sqrt{r^2 + L^2} \geq \frac{r+L}{\sqrt{2}}$ , which is tight when  $r$  is relatively small, i.e.,  $v_1 \leq r \leq v_2$ .
- $w = \sqrt{r^2 + L^2} \geq r$ , which is tight when  $r$  is relatively large, i.e.,  $r > v_2$ .

The above three lower bounds meet at  $v_1$  and  $v_2$ , which are defined as the switch points in (42). For example, when  $L = 8.5$  m, the proposed approximation of  $w$  is shown in Fig. 11, and the maximum absolute error of the approximation is merely around 1.5 m.

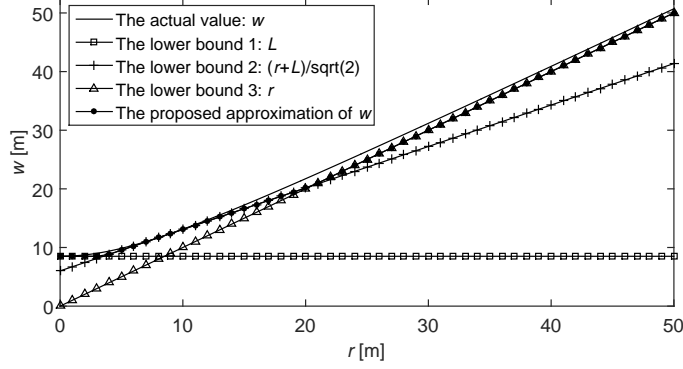


Fig. 11. Illustration of the proposed approximation  $w \approx \tilde{w}$ .

In the following, we show the computation of  $T_1^L$  as an example on how to obtain  $\{T_n^{Path}\}$  in  $p^{\text{cov}}(\lambda, \gamma)$  using the proposed approximation of  $w \approx \tilde{w}$  in (42).

From Theorem 1, for the range of  $0 < r \leq \sqrt{d_1^2 - L^2}$ ,  $T_1^L$  can be calculated by

$$T_1^L = \int_0^{\sqrt{d_1^2 - L^2}} \exp\left(-\frac{\gamma(\sqrt{r^2 + L^2})^{\alpha^L} P_N}{P A^L}\right) \mathcal{L}_{I_{\text{agg}}}^L\left(\frac{\gamma(\sqrt{r^2 + L^2})^{\alpha^L}}{P A^L}\right) f_{R,1}^L(r) dr, \quad (43)$$

where  $\zeta_1^L(w) = A^L w^{-\alpha^L}$  from (22) has been plugged into (43) and  $\mathcal{L}_{I_{\text{agg}}}^L(s)$  is the Laplace transform of  $I_{\text{agg}}$  for the LoS signal transmission evaluated at  $s$ .

In (43), according to Theorem 1 and (23),  $f_{R,1}^L(r)$  can be derived as

$$\begin{aligned} &= \exp\left(-\int_0^{r_1} \lambda \frac{\sqrt{u^2 + L^2}}{d_1} 2\pi u du\right) \exp\left(-\int_0^r \lambda \left(1 - \frac{\sqrt{u^2 + L^2}}{d_1}\right) 2\pi u du\right) \\ &\quad \times \left(1 - \frac{\sqrt{r^2 + L^2}}{d_1}\right) 2\pi r \lambda \\ &= \exp\left(-\frac{2\pi\lambda}{3d_1} \left((r_1^2 + L^2)^{3/2} - L^3\right)\right) \exp\left(-\pi\lambda r^2 + \frac{2\pi\lambda}{3d_1} \left((r^2 + L^2)^{3/2} - L^3\right)\right) \\ &\quad \times \left(1 - \frac{\sqrt{r^2 + L^2}}{d_1}\right) 2\pi r \lambda, \quad \left(0 < r \leq \sqrt{d_1^2 - L^2}\right), \end{aligned} \quad (44)$$

where  $r_1 = \sqrt{\left(\frac{A^{\text{NL}}}{A^L}\right)^{\frac{2}{\alpha^{\text{NL}}}} (r^2 + L^2)^{\frac{\alpha^L}{\alpha^{\text{NL}}}} - L^2}$  according to (12).

Besides, according to Theorem 1,  $\mathcal{L}_{\text{agg}}^L(s)$  in (43) for the range of  $0 < r \leq \sqrt{d_1^2 - L^2}$  should be computed by plugging (22) and (23) into (16). Similar to [10], we need to break the integration interval into several segments according to (42) and repeatedly calculate the following two definite integrals:  $Q_1 = \int_a^b \frac{u}{1 + (sPA^{\text{Path}})^{-1} (\sqrt{u^2 + L^2})^{\alpha^{\text{Path}}}} du$ , and  $Q_2 = \int_a^b \frac{\sqrt{u^2 + L^2} u}{1 + (sPA^{\text{Path}})^{-1} (\sqrt{u^2 + L^2})^{\alpha^{\text{Path}}}} du$ , where the string variable  $\text{Path}$  takes the value of “L” and “NL” for the LoS and the NLoS cases, respectively.

In the following, we discuss the computation of  $Q_1$  and  $Q_2$  for four cases.

**Case 1:** When  $a \geq 0$  and  $b \leq v_1$ , we invoke  $\sqrt{u^2 + L^2} \approx L$  according to (42). Thus,  $Q_1$  and  $Q_2$  can be written in closed-form expressions as

$$Q_1 \approx \frac{\frac{1}{2}(b^2 - a^2)}{1 + (sPA^{\text{Path}})^{-1} L^{\alpha^{\text{Path}}}} du, \quad (45)$$

and

$$Q_2 \approx \frac{\frac{1}{2}L(b^2 - a^2)}{1 + (sPA^{\text{Path}})^{-1} L^{\alpha^{\text{Path}}}} du. \quad (46)$$

**Case 2:** When  $a \geq v_1$  and  $b \leq v_2$ , we invoke  $\sqrt{u^2 + L^2} \approx \frac{u+L}{\sqrt{2}}$  according to (42). Thus,  $Q_1$  and  $Q_2$  can be written in closed-form expressions as

$$Q_1 \approx \int_a^b \frac{u}{1 + (sPA^{\text{Path}})^{-1} \left(\frac{u+L}{\sqrt{2}}\right)^{\alpha^{\text{Path}}}} du \quad (47)$$

$$= \int_{a+L}^{b+L} \frac{\tilde{u} - L}{1 + (sPA^{\text{Path}})^{-1} (\sqrt{2})^{-\alpha^{\text{Path}}} \tilde{u}^{\alpha^{\text{Path}}}} d\tilde{u} \quad (48)$$

$$= \rho_1(\alpha^{\text{Path}}, 1, t^{\text{Path}}, b+L) - \rho_1(\alpha^{\text{Path}}, 1, t^{\text{Path}}, a+L) \\ - L [\rho_1(\alpha^{\text{Path}}, 0, t^{\text{Path}}, b+L) - \rho_1(\alpha^{\text{Path}}, 0, t^{\text{Path}}, a+L)], \quad (49)$$

and

$$Q_2 \approx \int_a^b \frac{\frac{u+L}{\sqrt{2}} u}{1 + (sPA^{\text{Path}})^{-1} \left(\frac{u+L}{\sqrt{2}}\right)^{\alpha^{\text{Path}}}} du \quad (50)$$

$$= \int_{a+L}^{b+L} \frac{\frac{1}{\sqrt{2}} \tilde{u}^2 - \frac{L}{\sqrt{2}} \tilde{u}}{1 + (sPA^{\text{Path}})^{-1} (\sqrt{2})^{-\alpha^{\text{Path}}} \tilde{u}^{\alpha^{\text{Path}}}} d\tilde{u} \quad (51)$$

$$= \frac{1}{\sqrt{2}} [\rho_1(\alpha^{\text{Path}}, 2, t^{\text{Path}}, b+L) - \rho_1(\alpha^{\text{Path}}, 2, t^{\text{Path}}, a+L)] \\ - \frac{L}{\sqrt{2}} [\rho_1(\alpha^{\text{Path}}, 1, t^{\text{Path}}, b+L) - \rho_1(\alpha^{\text{Path}}, 1, t^{\text{Path}}, a+L)], \quad (52)$$

where  $\sqrt{u^2 + L^2} \approx \frac{u+L}{\sqrt{2}}$  is plugged into (47) and (50), the variable change of  $\tilde{u} = u + L$  is



performed in (48) and (51),  $t^{Path} = (sPA^{Path})^{-1} (\sqrt{2})^{-\alpha^{Path}}$ , and

$$\rho_1(\alpha, \beta, t, d) = \int_0^d \frac{u^\beta}{1 + tu^\alpha} du = \left[ \frac{d^{(\beta+1)}}{\beta+1} \right] {}_2F_1 \left[ 1, \frac{\beta+1}{\alpha}; 1 + \frac{\beta+1}{\alpha}; -td^\alpha \right], \quad (53)$$

where  ${}_2F_1[\cdot, \cdot; \cdot; \cdot]$  is the hyper-geometric function [24].

**Case 3:** When  $a \geq v_2$  and  $b < +\infty$ , we invoke  $\sqrt{u^2 + L^2} \approx u$  according to (42). Thus,  $Q_1$  and  $Q_2$  can be written in closed-form expressions as

$$Q_1 \approx \int_a^b \frac{u}{1 + (sPA^{Path})^{-1} u^{\alpha^{Path}}} du \quad (54)$$

$$= \rho_1(\alpha^{Path}, 1, (sPA^{Path})^{-1}, b) - \rho_1(\alpha^{Path}, 1, (sPA^{Path})^{-1}, a), \quad (55)$$

and

$$Q_2 \approx \int_a^b \frac{u^2}{1 + (sPA^{Path})^{-1} u^{\alpha^{Path}}} du \quad (56)$$

$$= \rho_1(\alpha^{Path}, 2, (sPA^{Path})^{-1}, b) - \rho_1(\alpha^{Path}, 2, (sPA^{Path})^{-1}, a), \quad (57)$$

where  $\sqrt{u^2 + L^2} \approx u$  is plugged into (54) and (56) and  $\rho_1(\alpha, \beta, t, d)$  is defined in (53).

**Case 4:** When  $a \geq v_2$  and  $b = +\infty$ ,  $Q_1$  and  $Q_2$  can then be expressed by

$$Q_1 \approx \int_a^{+\infty} \frac{u}{1 + (sPA^{Path})^{-1} u^{\alpha^{Path}}} du = \rho_2(\alpha^{Path}, 1, (sPA^{Path})^{-1}, a), \quad (58)$$

and

$$Q_2 \approx \int_a^{+\infty} \frac{u^2}{1 + (sPA^{Path})^{-1} u^{\alpha^{Path}}} du = \rho_2(\alpha^{Path}, 2, (sPA^{Path})^{-1}, a), \quad (59)$$

where

$$\begin{aligned} \rho_2(\alpha, \beta, t, d) &= \int_d^{+\infty} \frac{u^\beta}{1 + tu^\alpha} du \\ &= \left[ \frac{d^{-(\alpha-\beta-1)}}{t(\alpha-\beta-1)} \right] {}_2F_1 \left[ 1, 1 - \frac{\beta+1}{\alpha}; 2 - \frac{\beta+1}{\alpha}; -\frac{1}{td^\alpha} \right], (\alpha > \beta + 1). \end{aligned} \quad (60)$$

Plugging (22), (23) and (44) into (43), and with the help of (45), (46), (49), (52), (55), (57), (58), (59) when calculating  $\mathcal{L}_{I_{agg}}^L \left( \frac{\gamma(\sqrt{r^2 + L^2})^{\alpha^L}}{PAL} \right)$ , we can get  $T_1^L$  for 3GPP Case 1 using just one fold of integration shown in (43). The rest of  $\{T_n^{Path}\}$  for 3GPP Case 1 can be obtained in a very similar way as  $T_1^L$  and we omit the repetitive discussion for brevity.

## REFERENCES

- [1] ArrayComm & William Webb, Ofcom, London, U.K., 2007.
- [2] D. López-Pérez, M. Ding, H. Claussen, and A. Jafari, "Towards 1 Gbps/UE in cellular systems: Understanding ultra-dense small cell deployments," *IEEE Communications Surveys Tutorials*, vol. 17, no. 4, pp. 2078–2101, Jun. 2015.

- [3] 3GPP, “TR 36.872: Small cell enhancements for E-UTRA and E-UTRAN - Physical layer aspects,” Dec. 2013.
- [4] J. Andrews, F. Baccelli, and R. Ganti, “A tractable approach to coverage and rate in cellular networks,” *IEEE Transactions on Communications*, vol. 59, no. 11, pp. 3122–3134, Nov. 2011.
- [5] 3GPP, “TR 36.828: Further enhancements to LTE Time Division Duplex for Downlink-Uplink interference management and traffic adaptation,” Jun. 2012.
- [6] Spatial Channel Model AHG, “Subsection 3.5.3, Spatial Channel Model Text Description V6.0,” Apr. 2003.
- [7] X. Zhang and J. Andrews, “Downlink cellular network analysis with multi-slope path loss models,” *IEEE Transactions on Communications*, vol. 63, no. 5, pp. 1881–1894, May 2015.
- [8] T. Bai and R. Heath, “Coverage and rate analysis for millimeter-wave cellular networks,” *IEEE Transactions on Wireless Communications*, vol. 14, no. 2, pp. 1100–1114, Feb. 2015.
- [9] M. Ding, D. López-Pérez, G. Mao, P. Wang, and Z. Lin, “Will the area spectral efficiency monotonically grow as small cells go dense?” *IEEE GLOBECOM 2015*, pp. 1–7, Dec. 2015.
- [10] M. Ding, P. Wang, D. López-Pérez, G. Mao, and Z. Lin, “Performance impact of LoS and NLoS transmissions in dense cellular networks,” *IEEE Transactions on Wireless Communications*, vol. 15, no. 3, pp. 2365–2380, Mar. 2016.
- [11] 3GPP, “TR 36.814: Further advancements for E-UTRA physical layer aspects,” Mar. 2010.
- [12] M. Ding and D. López-Pérez, “Please lower small cell antenna heights in 5G,” *to appear in IEEE Globecom 2016*, Apr. 2016. [Online]. Available: [https://sites.google.com/site/mingding2016work/files/GC\\_3D\\_SGA.pdf](https://sites.google.com/site/mingding2016work/files/GC_3D_SGA.pdf)
- [13] H. S. Dhillon, R. K. Ganti, F. Baccelli, and J. G. Andrews, “Modeling and analysis of K-tier downlink heterogeneous cellular networks,” *IEEE Journal on Selected Areas in Communications*, vol. 30, no. 3, pp. 550–560, Apr. 2012.
- [14] M. D. Renzo, “Stochastic geometry modeling and analysis of multi-tier millimeter wave cellular networks,” *IEEE Transactions on Wireless Communications*, vol. 14, no. 9, pp. 5038–5057, Sep. 2015.
- [15] M. D. Renzo, W. Lu, and P. Guan, “The intensity matching approach: A tractable stochastic geometry approximation to system-level analysis of cellular networks,” *IEEE Transactions on Wireless Communications*, vol. 15, no. 9, pp. 5963–5983, Sep. 2016.
- [16] I. Bekmezci, O. K. Sahingoz, and S. Temel, “Flying Ad-Hoc networks (FANETs): A survey,” *Ad Hoc Networks*, vol. 11, no. 3, pp. 1254–1270, Jan. 2013.
- [17] F. Jiang and A. L. Swindlehurst, “Optimization of UAV heading for the ground-to-air uplink,” *IEEE Journal on Selected Areas in Communications*, vol. 30, no. 5, pp. 993–1005, June 2012.
- [18] M. Mozaffari, W. Saad, M. Bennis, and M. Debbah, “Drone small cells in the clouds: Design, deployment and performance analysis,” *arXiv:1509.01655 [cs.IT]*, Sep. 2015. [Online]. Available: <http://arxiv.org/abs/1509.01655>
- [19] P. Madhusudhanan, J. G. Restrepo, Y. Liu, T. X. Brown, and K. R. Baker, “Downlink performance analysis for a generalized shotgun cellular system,” *IEEE Transactions on Wireless Communications*, vol. 13, no. 12, pp. 6684–6696, Dec. 2014.
- [20] A. H. Jafari, M. Ding, D. Lopez-Perez, and J. Zhang, “Performance impact of LOS and NLOS transmissions in dense cellular networks under Rician fading,” *arXiv:1610.09256 [cs.IT]*, Oct. 2016. [Online]. Available: <http://arxiv.org/abs/1610.09256>
- [21] X. Li, R. W. Heath, Jr., K. Linehan, and R. Butler, “Impact of metro cell antenna pattern and downtilt in heterogeneous networks,” *arXiv:1502.05782 [cs.IT]*, Feb. 2015. [Online]. Available: <http://arxiv.org/abs/1502.05782>
- [22] G. Fischer, F. Pivit, and W. Wiesbeck, “Microwave conference, 2002. 32nd european,” pp. 1–4, Sep. 2002.

- [23] T. K. Sarkar, Z. Ji, K. Kim, A. Medouri, and M. Salazar-Palma, "A survey of various propagation models for mobile communication," *IEEE Antennas and Propagation Magazine*, vol. 45, no. 3, pp. 51–82, Jun. 2003.
- [24] I. Gradshteyn and I. Ryzhik, *Table of Integrals, Series, and Products (7th Ed.)*. Academic Press, 2007.